



Solvothermal synthesis and photocatalytic performance of Mn⁴⁺-doped anatase nanoplates with exposed {001} facets

Maria-Veronica Sofianou^a, Maria Tassi^a, Vassilis Psycharis^a, Nikos Boukos^a, Stavros Thanos^a, Tiverios Vaimakis^b, Jiaguo Yu^c, Christos Trapalis^{a,*}

^a Institute of Advanced Materials, Physicochemical Processes, Nanotechnology and Microsystems, National Center for Scientific Research "Demokritos", 153 10 Attiki, Greece

^b Department of Chemistry, University of Ioannina, 451 10, Ioannina, Greece

^c State Key Laboratory for Advanced Technology Materials Synthesis & Processing, Wuhan University of Technology, Wuhan 430070, People's Republic of China

ARTICLE INFO

Article history:

Received 18 February 2014

Received in revised form 24 May 2014

Accepted 29 May 2014

Available online 5 June 2014

Keywords:

Mn⁴⁺/TiO₂

Anatase nanoplates

{001} facets

Photocatalysis

NO oxidation

Acetaldehyde decomposition

ABSTRACT

The photocatalytic activity of TiO₂ and manganese doped TiO₂ nanoplates with various manganese atomic percentages, in the range of 2–7%, was studied. The undoped and doped nanoplates with exposed {001} facets were produced by a solvothermal method. The crystal structure as well as the shape of the TiO₂ and Mn⁴⁺/TiO₂ anatase nanoparticles was determined with X-ray powder diffraction (XRD) and transmission electron microscopy (TEM). Both techniques revealed that the nanocrystals are in the form of plates. Moreover, the anisotropic peak broadening of the X-ray diffraction patterns was studied using the Rietveld refining method. Chemical analysis of the photocatalyst that was carried out with X-ray photoelectron spectroscopy (XPS) showed the presence of manganese ions in the TiO₂ anatase matrix. The Density Functional Theory (DFT) calculations exhibited a decrease in the energy gap and an increase in the density of the electronic states inside the gap for the doped TiO₂. These observations were in agreement with the results of the UV–visible diffuse reflectance spectroscopy (DRS) that demonstrated an adsorption shift towards the visible region for the same samples.

The photocatalytic activity of the synthesized catalysts was investigated by the photocatalytic oxidation of the gaseous nitric oxide (NO) and decomposition of the gaseous acetaldehyde (CH₃CHO) under visible light irradiation. The optimal concentration of dopant that improves the photocatalytic activity of the nanoplates was determined.

© 2014 Elsevier B.V. All rights reserved.

1. Introduction

Titanium dioxide (TiO₂), also known as titania, is an extensively studied oxide semiconductor photocatalysts. The anatase phase of titania has been proven to be among other various oxide semiconductors the most suitable photocatalyst for environmental applications due to its nontoxicity, low cost, strong oxidizing power and long term stability against photocorrosion and chemical corrosion [1–4].

However, its relatively large wide band gap (~3.2 eV) and the high recombination rate of the photogenerated electron and hole pairs hinders its applications [5]. Therefore, considerably efforts

have been made in order to narrow the anatase band gap towards the visible region of the light spectrum. Some of these several band gap modifications have been suggested such as fabricating composites with other oxide semiconductors, sensitizing with low band semiconductors, adding nonmetals or metal ions [6–9]. One of the most efficient way to make the TiO₂ anatase active under visible light is doping or surface modification with transition metal cations or their oxides [10–15]. It has also been proven that the transition metal dopants also inhibit the photogenerated charge recombination as the metal sites are considered to act as trapping site by accepting the photogenerated electrons from the TiO₂ valance band [16,17]. Moreover, several theoretical and experimental studies have shown that the {001} surface of the anatase crystal is more reactive than the {101} surface [18,19]. This implies that TiO₂ anatase structures with exposed {001} crystal facets doped with transition metal ions will achieve high photocatalytic activity.

This study reports the synthetic procedure of manganese ion doped TiO₂ anatase crystalline structures in the form of nanoplates

* Corresponding author at: Institute of Advanced Materials, Physicochemical Processes, Nanotechnology and Microsystems, NCSR "Demokritos", 153 10 Ag. Paraskevi, Attiki, Greece. Tel.: +30 210 650 3343; fax: +30 210 651 9430.

E-mail address: trapalis@ims.demokritos.gr (C. Trapalis).

with exposed highly reactive {001} facets and evaluates the influence of the structure and the percentage of dopant on their photocatalytic activity in decomposing the acetaldehyde gas and oxidizing the NO gas, which both are prominent air pollutants. The manganese exists in Mn^{4+} oxidation state in the anatase nanoplates, extending the light absorption range and significantly enhancing their photocatalytic activity under visible light irradiation. The photocatalytic activity of the different anatase structures is evaluated by comparing their photonic efficiencies that were calculated from the amount of the acetaldehyde gas decomposed and NO gas oxidized to NO_2 and NO_3^- .

2. Materials and methods

2.1. Synthesis of TiO_2 and $\text{Mn}^{4+}/\text{TiO}_2$ anatase samples

Pure TiO_2 and $\text{Mn}^{4+}/\text{TiO}_2$ anatase nanoplates with exposed {001} crystal facets were fabricated using a solvothermal method. For the fabrication of the pure TiO_2 nanoplates, 3 mmol of titanium isopropoxide $[\text{Ti}(\text{C}_3\text{H}_7\text{O})_4]$ from Alfa Aesar Chemicals were dissolved into 50 ml of absolute ethanol from Merck under vigorous stirring at room temperature. Then 0.6 ml (0.03 mol) of hydrofluoric acid (HF 40%) from Merck was added into the above solution. HF acts as a capping agent and is responsible for the dominant formation of the {001} facets of the anatase crystal. The final solution was poured into a 60 ml Teflon-lined autoclave until 80% of its volume was filled and was placed into the oven for 24 h at 180 °C. The as prepared sample was collected through centrifugation of the solution. In order to obtain fluoride free TiO_2 anatase nanoplates, with no adsorbed fluoride atoms on their {001} crystal facets, the collected powder product was washed 3 times with distilled water and then was dispersed in 50 ml of 5 M NaOH aqueous solution and stirred for approximately 30 min. The dispersion was centrifuged and washed several times until the pH reached 7. The washed samples were dried in a furnace at 70 °C overnight. The manganese doped samples were prepared with the same procedure as the pure sample. A concentration of manganese nitrate $[\text{Mn}(\text{NO}_3)_2 \cdot 4\text{H}_2\text{O}$ 99%] from Aldrich was added to the calculated amount of TiO_2 in order to get the dopant concentration within the range of 2–7 at%.

2.2. Characterization techniques

The structure of the pure TiO_2 and $\text{Mn}^{4+}/\text{TiO}_2$ anatase samples was examined by X-ray diffractometry (SIEMENS D500 diffractometer) using $\text{Cu K}\alpha$ radiation. The measurements were performed using the following combination of slits: $1.0^\circ/1.0^\circ/1.0^\circ$ as aperture diaphragms, 0.15° as detector diaphragm, and 0.15° as diffracted beam monochromator diaphragm. The measured 2θ range between 20° and 70° was scanned in steps of $0.03^\circ/10\text{ s}$. The accelerating voltage and applied current were 40 kV and 35 mA, correspondingly. The identification of the patterns was done with the cards of the International Centre for Diffraction Data. The Rietveld method using the FullProf program was applied for the analysis of the pure and manganese doped anatase samples [20]. Morphological observations were carried out with a transmission electron microscope (Philips CM20) operated at 200 kV and equipped with a Gatan GIF200 image filter. The TEM specimens of all samples were prepared by direct deposition on a carbon coated Cu TEM grid. X-ray photoelectron spectroscopy (XPS) measurements of the $\text{Mn}^{4+}/\text{TiO}_2$ anatase nanoplates were carried out in an ultra-high vacuum using a VG ESCALAB 210 electron spectrometer equipped with a multichannel detector. The spectra were excited using $\text{Mg K}\alpha$ (1253.6 eV) radiation (operated at 200 W) of a twin anode in the constant analyzer energy mode with pass energy of 30 eV. All the binding energies were referred to the

C 1s peak at 284.8 eV and to the O 1s peak at 530.2 eV of the surface adventitious carbon and oxygen respectively. UV–vis diffuse reflectance spectra of all samples were obtained from the dry-pressed film samples using a UV–vis spectrometer (UV-2100, Shimadzu, Japan) with an integrating sphere attachment for their reflectance in the wavelength range 200–900 nm. BaSO_4 was used as a reflectance standard. The widths of the effective band gaps of the samples were determined using Kubelka–Munk phenomenological theory. The theoretical study of the energy band gaps of the Mn^{4+} -doped anatase structure of titanium dioxide Ti_2O was performed using the Density-Functional Theory (DFT) [21,22] and the numerical calculations were implemented with the Quantum Espresso code [23]. The Kohn–Sham wavefunctions were expanded into a plane wave basis set with an energy cutoff of 32 Ryd. Additionally, the Vanderbilt ultrasoft pseudopotentials calculated with Perdew–Burke–Ernzerhof (PBE) exchange–correlation functional were used for all the atoms, Ti, O and Mn. Also, the Local Density Approximation (LDA) [24] with Hubbard, factor U, correction (LDA+U) was used in order to obtain the improvement of band structure. The factor U was chosen to be 8 eV. The proper choice has been made after the calculation of the energy band gap of anatase with different values of U, and it was found that, for this value, the evaluated band gap is 3.24 eV, which is close to the experimental value 3.239 eV [25]. The structures modelled using supercells of anatase in which a Mn atom, in different proportions, had substituted a Ti atom. Specifically, 4 and 12 cells were used in order to have atomic ratios of Mn/Ti such as 1/16 and 1/48, respectively. The lattice parameters were $a=b=3.785\text{ \AA}$ and $c=38.056\text{ \AA}$ and 114.168 Å for the 4 and 12 cells, respectively. After the relaxation of the structures the a and b lattice parameters were the same but the third lattice parameter was decreased and became $c=35.859\text{ \AA}$ and $c=111.652\text{ \AA}$ for the 4 and 12 cells, respectively.

2.3. Evaluation of the photocatalytic activity

The photocatalytic activity of all samples was studied in the oxidation of the NO gas following a modified ISO standard ISO/DIS 22197-1 and in the acetaldehyde gas decomposition [26]. The samples were pressed in sample holders with an apparent surface area of 20 cm^2 and then were pre-illuminated under a UV-A lamp with a light irradiance of 10 W m^{-2} for three days in order to remove all possible organic residual compounds from the sample's surfaces. After the pre-illumination period the sample holders containing the TiO_2 and $\text{Mn}^{4+}/\text{TiO}_2$ powders were placed into the flow-type photoreactor with their surface parallel to an optical quartz window and were illuminated by UV-A radiation. The sample holders were separated from the window by a 5 mm thick air layer. The test gas passed only through the space between the sample holder and the window. The reactor is fabricated from materials that adsorb minimal NO or acetaldehyde gas and withstand irradiation of near-UV light. The samples were exposed to model air containing 1 ppm nitric oxide (NO) or 70 ppm acetaldehyde (CH_3CHO). The photocatalyst adsorbs and oxidizes the NO to NO_2 and NO_3^- on its surface. In the case of the acetaldehyde it is also adsorbed on the photocatalyst surface and then decomposed. The performance of the photocatalyst is determined by the amount of the net removal of the nitrogen oxide (NO) or of the acetaldehyde. The photocatalytic activity of the samples was evaluated under visible light illumination with irradiance of 8000 lux for 60 min. The photonic efficiency ζ (%) of the samples for the NO oxidation/acetaldehyde decomposition was calculated using the Eq. (1):

$$\zeta = \frac{n_{\text{degraded molecules}}}{n_{\text{available photons}}} = \frac{\int_{t_0}^{t_1} AX[\text{ppm}]dt}{q_{n,p}\Delta T} \times 100\% \quad (1)$$

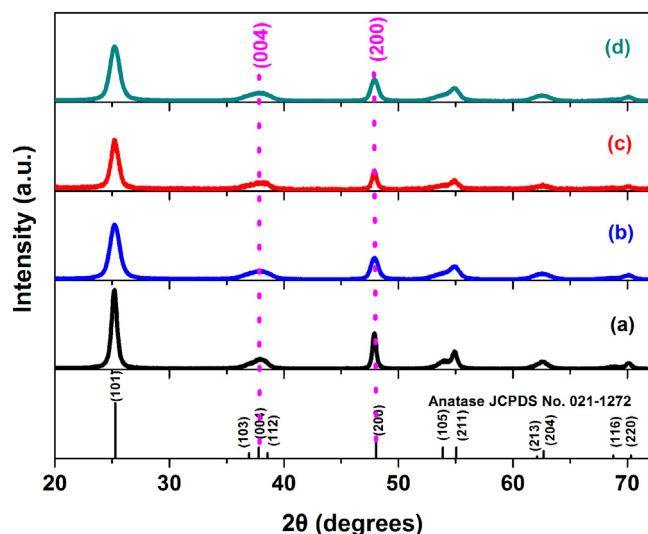


Fig. 1. XRD patterns of the pure TiO_2 (a), 2 at% $\text{Mn}^{4+}/\text{TiO}_2$ (b), 6 at% $\text{Mn}^{4+}/\text{TiO}_2$ (c), 7 at% $\text{Mn}^{4+}/\text{TiO}_2$ anatase nanoplates (d).

where, t_0 is the time moment when the visible light was switched on, t_1 is the time moment at the end of the illumination, ΔT is determined by equation $\Delta T = t_1 - t_0$, A is the coefficient taken as a product of the gas flow value (3 L min^{-1} for NO and 115 mL min^{-1} for acetaldehyde) and of the value 10^{-6} expressed in mol s^{-1} ($A = 2.08 \times 10^{-9} \text{ mol s}^{-1}$ for NO and $A = 0.69 \times 10^{-9} \text{ mol s}^{-1}$ for acetaldehyde), X (taken in ppm) is either the difference between the initial NO/NO_x concentration ($\sim 1 \text{ ppm}$) and the monitored NO/NO_x concentration or the directly monitored NO_2 concentration. In the case of the acetaldehyde it is the difference between the initial acetaldehyde concentration ($\sim 70 \text{ ppm}$) and the monitored acetaldehyde concentration. Lastly, $q_{n,p}$ is the photon flux of the samples' surface S (expressed in mol s^{-1}).

The photon flux of the sample's surface (mol s^{-1}) can be calculated using the Eq. (2):

$$q_{n,p} = \frac{E\lambda S}{N_A hc}, \quad (2)$$

where, E is the irradiance (W m^{-2}), S is the apparent surface area (m^2), λ is the wavelength (m), N_A is the Avogadro constant (mol^{-1}), h is Planck's constant (J s) and c is the speed of light (m s^{-1}).

The rate of the gas flow, with 50% relative humidity, into the flow-type photoreactor was 3 L min^{-1} for the NO gas and 115 mL min^{-1} for the acetaldehyde gas. The photonic efficiency of the monitored NO, NO_2 , NO_x , acetaldehyde gases was calculated at the end of the illuminating period of time.

3. Results and discussion

3.1. Phase observations and Rietveld refinements

The XRD patterns of the TiO_2 and $\text{Mn}^{4+}/\text{TiO}_2$ samples are presented in Fig. 1. The crystalline phase of all samples is only anatase [JCPDS No. 021-1272 card]. This indicates that the Mn^{4+} ions are well dispersed in the TiO_2 nanocrystals and did not influence their crystal patterns. Moreover, no reflections were detected regarding either the formation of another phase such as rutile, brookite or the presence of any impurities of the remaining precursor used each time. The observed peak broadening of the (004) reflection and the narrower peak of the (200) reflection is attributed to the anisotropic growth of the crystals along the c -axis of the anatase lattice. This peak broadening is related to the very small dimension of crystallites along the c -axis, in the contrary, the observed

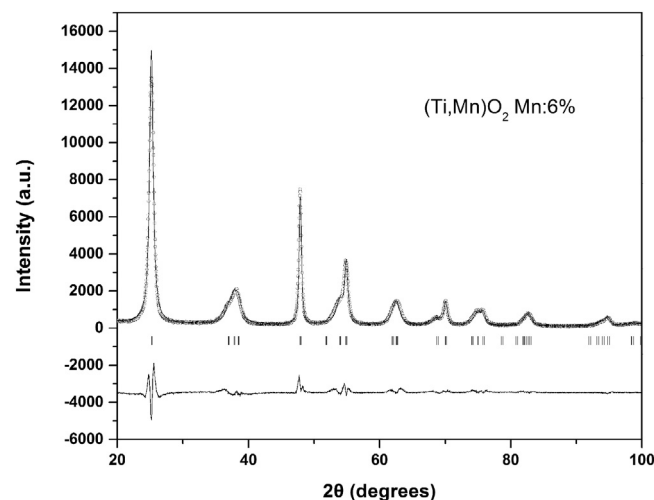


Fig. 2. XRD spectrum of sample 6 at% $\text{Mn}^{4+}/\text{TiO}_2$ refined by the Rietveld method. (○) Experimental points, the continuous line correspond to the calculated spectrum, vertical bars (|) at the bottom indicate the position of Bragg peaks. The continuous line at the bottom is the difference between the experimental intensity values and the calculated one.

narrower peaks are due to the dimension along the a -axis, which is bigger in relation to the c -axis size of the nanocrystals [27–29]. This indicates that the crystals are in the form of plates. Furthermore, from the XRD patterns regarding the Mn^{4+} doped anatase samples (Fig. 1(b–d)), the (101) diffraction peak broadens as the manganese ion concentration increases because of the systematic decrease of the nanoplates. This observation comes also in agreement with the Rietveld analysis of these samples as well as their corresponding TEM micrographs which will be presented further down. Fig. 2 presents the XRD spectrum of sample 6 at% $\text{Mn}^{4+}/\text{TiO}_2$ refined by the Rietveld method. According to Rietveld calculations of the pure anatase sample the longest and shortest apparent size of the nanoplates is 43.100 nm and 7.634 nm respectively. The longest apparent size of the 2, 6 and 7 at% Mn^{4+} doped anatase samples is 15.488 nm, 31.742 nm and 23.727 nm correspondingly, whereas their shortest apparent size is 4.368 nm, 4.685 nm and 4.828 nm, respectively. This suppress crystal growth is known from the literature that is caused by the incorporated Mn^{4+} ions in the TiO_2 anatase lattice as they interfere into the intergranules that inhibit the grain boundary mobility or alter the surface energy leading to a decrease in grain growth velocity or nucleation energy obstruction resulting in decrease in grain size [30–32]. Table 1 lists the unit cell dimensions and the agreement factors for all studied samples [33]. The variation of unit cell dimensions upon Mn^{4+} substitution are not significant (less than 0.5% for all parameters).

3.2. Morphological observations

The TEM micrographs of the pure and Mn^{4+} doped TiO_2 anatase samples are presented in Fig. 3(a–h). As it can be noticed their crystal habit is in the form of nanoplates. The large square surface areas of the nanoplates are the {001} crystal facets and the small isosceles trapezoidal surfaces are the {101} crystal facets (Fig. 3(e)). The high-resolution TEM micrograph of the nanoplate lying on the TEM grid (Fig. 3(f)) shows that their lattice fringes with spacing of 0.352 nm corresponds to the (101) planes of anatase [34]. Furthermore, the other high-resolution TEM micrograph (Fig. 3(g)) directly reveals that the lattice spacing parallel to the top and bottom facets is 0.235 nm that corresponds to the (001) planes of the anatase crystal, indicating that the top and bottom facets of the nanoplates are the (001) and (001) planes, respectively [34].

Table 1
Unit cell dimensions and agreement factors for the series of the pure TiO₂ and Mn⁴⁺ doped nanoplates.

Sample	<i>a</i> (Å)	<i>c</i> (Å)	<i>V</i> (Å ³)	<i>R</i> _p	<i>R</i> _{wp}	<i>R</i> _B
TiO ₂	3.78479(3)	9.51237(12)	136.26(1)	–	–	–
Pure TiO ₂ our data	3.7939(1)	9.4963(6)	136.69(1)	13.3	18.2	7.83
2 at% Mn ⁴⁺ /TiO ₂	3.7959(2)	9.5017(8)	136.91(1)	12.0	14.7	7.32
6 at% Mn ⁴⁺ /TiO ₂	3.7977(1)	9.5077(6)	137.13(1)	9.09	11.3	5.31
7 at% Mn ⁴⁺ /TiO ₂	3.7974(1)	9.5074(7)	137.10(1)	10.1	12.5	4.53

The corresponding SAED pattern (Fig. 3(h)) also confirms that the faceted surface is the (001) surface as the square shaped plane is a single crystal, with zone axis [001]. After the crystal growth process of the anatase nanoplates, doped with manganese ions, the morphological structure of the nanoplates is almost identical as the pure anatase samples. More specifically, their crystal habit has remained in the form of plates with the only difference compared to the pure nanoplates is that their crystal size has slightly decreased with the increase of Mn⁴⁺ content in the anatase lattice (Fig. 3(b–d)). The longest and shortest average apparent size of the pure nanoplates is 42.2 nm and 7.2 nm, respectively. As for the 2, 6 and 7 at% Mn⁴⁺ doped anatase nanoplates the longest average apparent size is 14.78 nm, 30 nm and 22 nm, respectively, whereas the shorted average apparent size of the nanoplates is 4.15 nm, 4.32 nm and 4.3 nm correspondingly. These observations come in agreement with the calculated apparent sizes of the nanoplates using the Rietveld refining method that where mentioned in Section 3.1.

3.3. XPS analysis

XPS measurements were carried out in order to confirm the presence of manganese ions and also to investigate the oxidation state of the ions present in the anatase samples. The Ti 2p, O 1s and Mn 2p core level of the anatase sample with the lowest manganese ion atomic percentage (2 at% Mn⁴⁺/TiO₂) is present in Fig. 4. The XPS observations show that only O, Ti, Mn elements were detected from the samples in spectrum analysis. The O 1s peak appearing at

532.6 eV (Fig. 4(a)) is attributed to the hydroxyl groups arising from the chemisorbed water [30,35]. It is mentioned in literature that the presence of the oxygen peak at 531.9–532.62 is developed with the increasing of the oxygen vacancies that are created to maintain the charge neutrality when the local electrostatic bond is broken [35]. The Ti 2p_{1/2} and Ti 2p_{3/2} peak that are present in Fig. 4(b) correspond to the binding energies at 459.8 eV and 465.6 eV, respectively. These peaks are attributed to Ti⁴⁺. The binding energies of Ti 2p_{1/2} and Ti 2p_{3/2} of pure TiO₂ samples are located at 459.8 eV and 464.0 eV correspondingly [36,37]. This slightly positive shift for the Mn⁴⁺/TiO₂ sample is caused by the presence of Mn⁴⁺ in the anatase lattice [37]. As for Mn2p_{3/2} peak with the binding energy at 642.4 eV originates from the Mn⁴⁺ [38–40]. No fluoride binding energy peak was evident in the sample which indicates that the adsorbed fluoride atoms on the {001} crystal facets were entirely removed during their surface cleaning procedures with a NaOH washing aqueous solution.

3.4. UV–vis spectra and DFT calculations

The determination of the band gap of the pure and Mn⁴⁺ doped anatase samples was evaluated using the Kubelka–Munk method based on the diffuse reflectance spectra [41]. The $(F(R) \times E)^{1/2}$ versus *E* (eV) plots of the samples are presented in Fig. 5, where $F(R) = (1 - R)^2/2R$, *R* is the diffuse reflectance of the sample relative to the reflectance of the standard BaSO₄. The band gap energies *E*_g were obtained by extrapolating the linear portion (*F*(*R*) = 0) of the curve onto the *x*-axis. As can be seen the pure anatase nanoplates

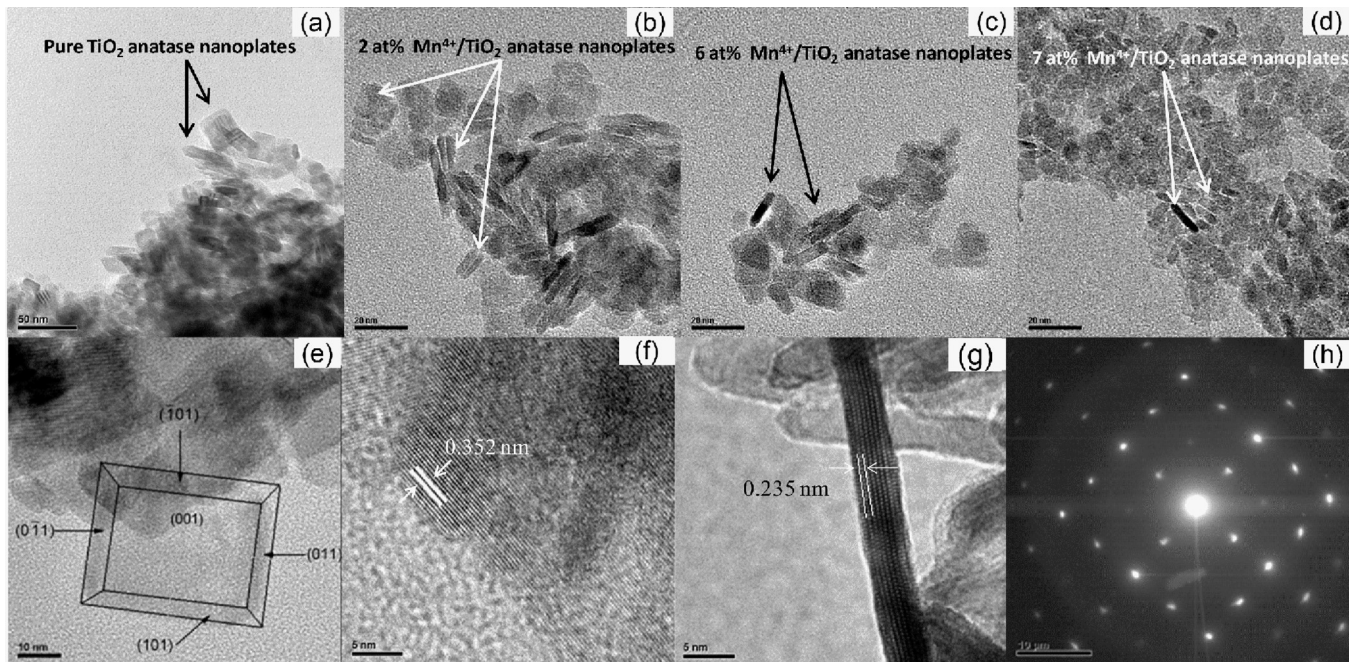


Fig. 3. TEM micrographs of the pure TiO₂ anatase nanoplates (a, e), 2 at% Mn⁴⁺/TiO₂ nanoplates (b), 6 at% Mn⁴⁺/TiO₂ nanoplates (c), 7 at% Mn⁴⁺/TiO₂ nanoplates (d), individual nanoplate recorded along [001] (f), individual nanoplate recorded along [010] (g), SAED pattern of the nanoplate (h).

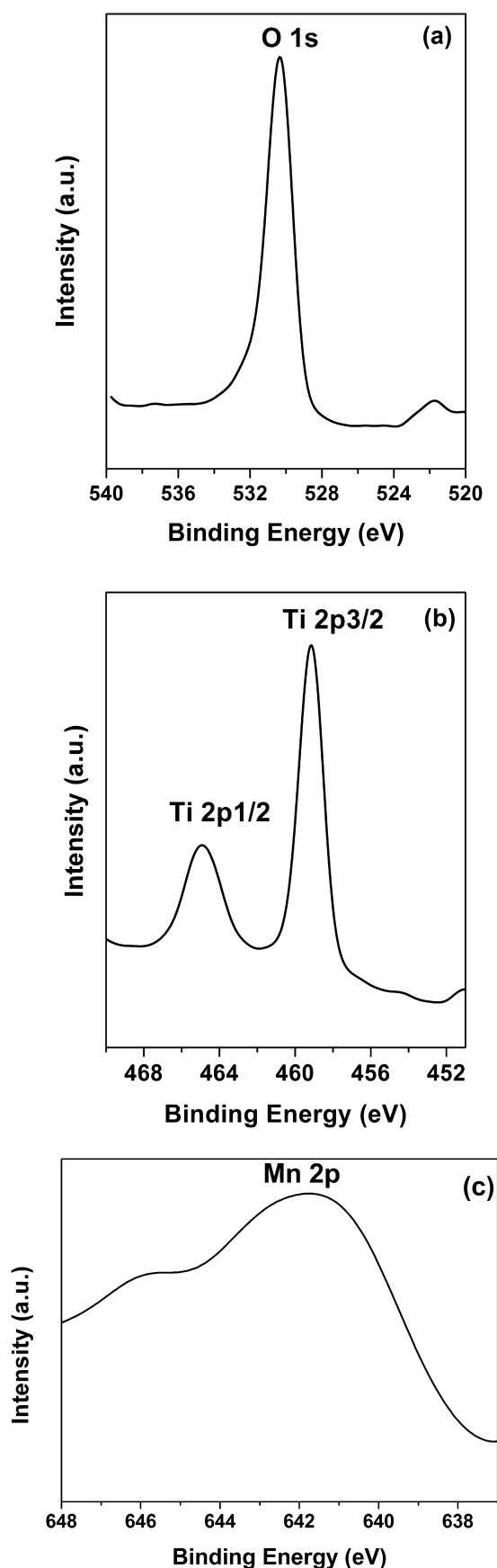


Fig. 4. High-resolution XPS spectrum of O 1s (a), Ti 2p_{1/2}, Ti 2p_{3/2} (b) and Mn 2p (c) of the sample containing the smallest amount of manganese (2 at% Mn⁴⁺/TiO₂).

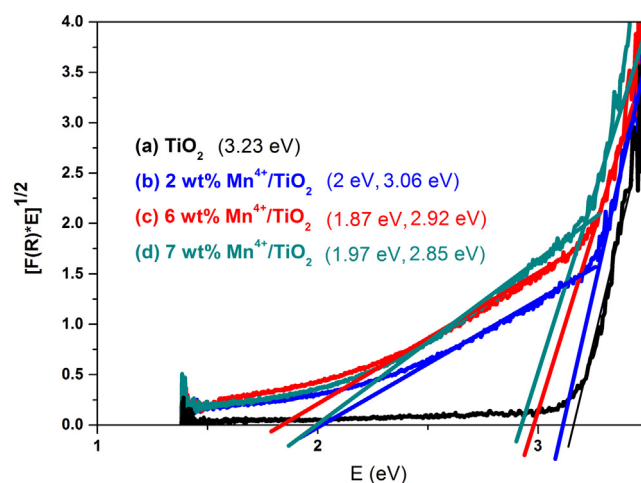


Fig. 5. $(F(R) \times E)^{1/2}$ versus E (eV) plots of the pure TiO₂ (a), 2 at% Mn⁴⁺/TiO₂ (b), 6 at% Mn⁴⁺/TiO₂ (c), 7 at% Mn⁴⁺/TiO₂ anatase nanoplates (d).

absorb around 400 nm due to the band gap absorption of anatase TiO₂, which is ~ 3.2 eV. More specifically, the pure anatase crystals have an energy gap at 3.23 eV (Fig. 5(a)). For the Mn⁴⁺ doped anatase samples two adsorption edges are present due to existence of electronic states inside the gap [42]. The 2, 6 and 7 at% Mn⁴⁺/TiO₂ anatase nanoplates have a first adsorption end at 3.06, 2.92 and 2.85 eV, respectively and a second one at 2, 1.87 and 1.97 eV (Fig. 5(b–d)). This result from the photocatalysis viewpoint is of great use as it is possible to tune the onset of the absorption to the desired visible wavelength by tuning the atomic percentage of Mn⁴⁺ ions into the anatase crystal.

The theoretical calculations of the energy gap of all samples were carried out according to the following actions. The structures were modelled using supercells of anatase in which a Mn atom, in different proportions, had substituted a Ti atom. Specifically, we used 4 and 12 cells in order to have atomic ratios of Mn/Ti such as 1/16 (6 at% Mn⁴⁺/TiO₂) and 1/48 (2 at% Mn⁴⁺/TiO₂), respectively. The formation of a cell as to achieve manganese atomic percentage of 7% was not plausible. In Fig. 6, the density of states for the valence and conduction bands for the pure and Mn⁴⁺ doped anatase samples is presented. Thus, one can easily see the existence of intermediate levels between the energies 8.4 and 9.4 eV for both manganese ion doped samples. According to theoretical calculations, these intermediate levels between the gap are probably due to the energy states that arise in the forbidden zone of energy caused by the presence of transition metals and oxygen vacancies in the TiO₂ lattice [15].

3.5. Photocatalytic activity

The photocatalytic activity of the pure and Mn⁴⁺ doped TiO₂ anatase nanoplates was evaluated by oxidizing the NO gas as well as decomposing the acetaldehyde gas. As it well known, when the photocatalyst is activated by light, in this case by visible light irradiation, an electron and hole pair is created (e^-/h^+):



It has been mentioned in some of our previous studies [43,44] that the electron that has migrated to the {101} crystal facets of the TiO₂ anatase nanoplates [18,19] reacts with the favourably adsorbed O₂ [45] on these specific facets forming superoxide anions (O₂⁻). As a base it will form HO₂ radicals with the traces of water that are originated from the humidity of the air flow and then it will further react with the NO gas that is adsorbed on the {101} crystal facets of the nanoplates, forming NO₂ and a hydroxyl

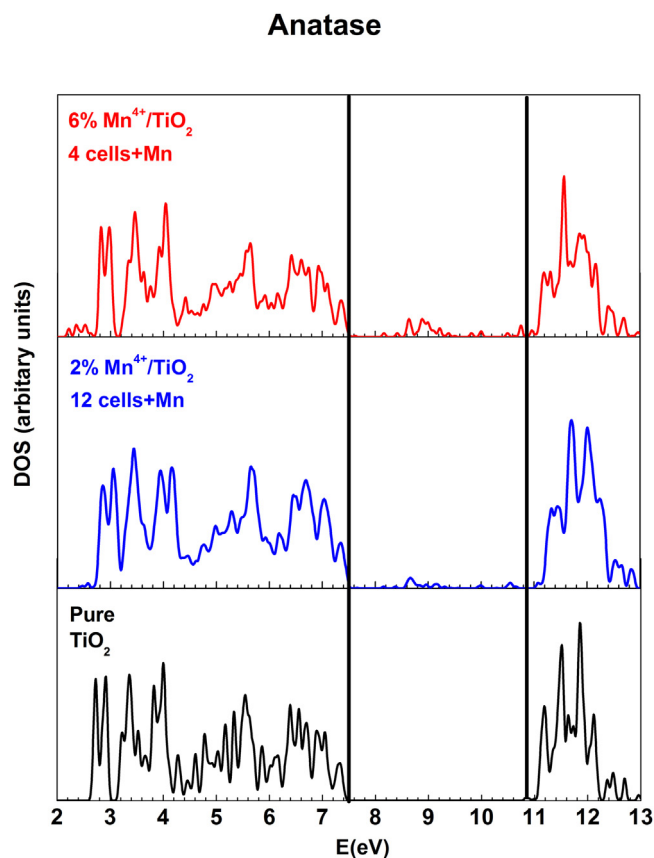


Fig. 6. Density of states for the pure and doped anatase samples.

radical. All nitrogen species (NO, NO₂) are photocatalytically oxidized leading to nitrate (NO₃[−]) whereas O₂ is photochemically reduced according to the following chemical reaction:



It has been widely reported that acetaldehyde is photocatalytically degraded either by the OH radicals or by the photogenerated

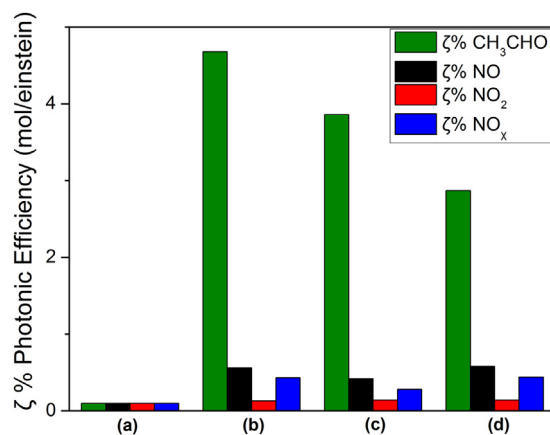
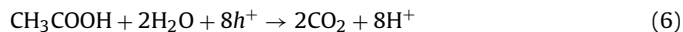
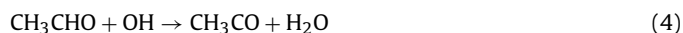


Fig. 8. Photonic efficiency of the pure TiO₂ (a), 2 at% Mn⁴⁺/TiO₂ (b), 6.0 at% Mn⁴⁺/TiO₂ (c), 7 at% Mn⁴⁺/TiO₂ anatase nanoplates (d) for NO oxidation and acetaldehyde decomposition.

holes according to the following chemical reactions [46–51] and with the assumption that the only radical species driving the photocatalytic degradation are the OH and the photogenerated holes:



These chemical reactions take place on the {001} facets of the nanoplates as the photogenerated holes migrate to these facets and react with the dissociated water molecules that are present creating active oxygen species, which have strong oxidative ability for many organic substances [46,47].

Fig. 7 shows the concentration profiles of the acetaldehyde gas and the NO, NO₂ and NO_x gases over the nanoplate's surface during their photocatalytic tests. Fig. 8 presents the photonic efficiencies of the studied doped samples and of the pure TiO₂ anatase nanoplates for NO oxidation and acetaldehyde decomposition. It

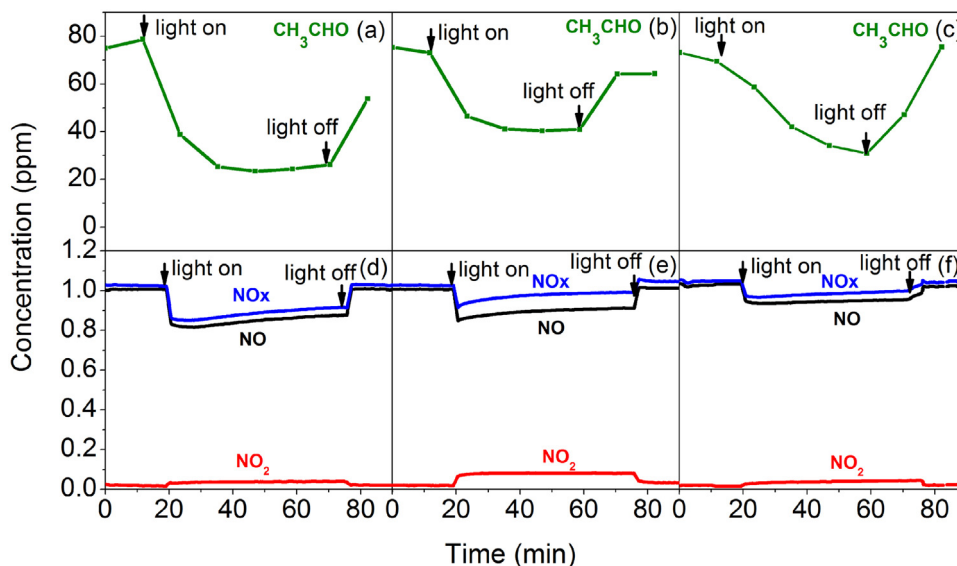


Fig. 7. Concentration profiles of acetaldehyde, NO, NO₂ and NO_x gases over the 2 at% Mn⁴⁺/TiO₂ (a and d), 6 at% Mn⁴⁺/TiO₂ (b and e), 7 at% Mn⁴⁺/TiO₂ anatase nanoplates (c and f).

can be noticed that the $\text{Mn}^{4+}/\text{TiO}_2$ nanoplates are photocatalytic active under visible light due to the presence of Mn^{4+} d states narrowing the band gap and allowing maximum adsorption of light in the visible region. Moreover, the dopant cation related trap states and oxygen vacancies restrain the photogenerated electrons and holes enhancing this way their photocatalytic activity. The pure anatase nanoplates have no photocatalytic activity under visible light as their maximum absorption is in the UV-A region therefore no sufficient number of electrons and holes can be produced in order either oxidize the NO gas or decompose the acetaldehyde gas. From Figs. 7 and 8 it is obvious that as the concentration of the transition metal dopant increases, the interfacial electron and hole transfer are inhibited and the photoactivity is reduced. This declination of the photonic efficiency is attributed to the extensive amount of the Mn^{4+} cations in the nanoplates as they become the recombination centers of the electron–hole pairs and reduce the separation efficiency of the photogenerated charges. Therefore, the 2 at% $\text{Mn}^{4+}/\text{TiO}_2$ sample shows higher photocatalytic activity than the others. All Mn^{4+} doped nanoplates showed higher photocatalytic activity in decomposing acetaldehyde gas in comparison to NO oxidation due to their dominant {001} facets and their large hole density.

4. Conclusions

In this study we have successfully prepared Mn^{4+} doped anatase nanoplates with exposed {001} facets by a simple solvothermal method. The XRD patterns revealed that the Bragg peak that corresponds to the (004) reflection of the TiO_2 and $\text{Mn}^{4+}/\text{TiO}_2$ samples is broad due to the anisotropic growth of the nanocrystals along the *c*-axis of the anatase lattice. This indicates that the *c*-axis is smaller than the *a*- and *b*-axis of the anatase lattice and the crystal habit of the samples is in the form of plates. TEM observations confirmed the remarks made from the XRD patterns of all samples that the {001} facets are dominant in comparison to the {101} facets of the anatase crystal and they have a plate like morphological structure. Rietveld refinement method was used to calculate the longest and shortest apparent length of the nanoplates. These calculations came in agreement with the measured average apparent sizes of the nanoplates from the TEM micrographs. The DRS analysis and DFT calculations showed that doping of Mn^{4+} into TiO_2 shifts the absorbance band of TiO_2 towards the visible light region and can be tailored according to the amount of manganese ions present in the anatase lattice. The incorporation of Mn^{4+} ions into the TiO_2 was evidenced by XPS analysis. Lastly, photocatalytic activity of anatase nanoplates doped with Mn^{4+} ions was achieved within the visible light range. The small amounts of manganese ion doping into the anatase lattice causes better separation of electrons and holes, allowing more efficient channelling to the surface of the nanoplates of the produced charge carriers, thus enhancing the photocatalytic activity in comparison to the TiO_2 nanoplates with higher dopant concentration.

Acknowledgements

This work was partially supported by the General Secretariat for Research and Technology of Greece under the projects 09SYN-42-925 ARISTON, 12SLO ET30 1162 and 12CHN205 PhotoTiGRA.

References

- [1] A. Fujishima, K. Honda, *Nature* 238 (1972) 37–38.
- [2] D.Q. Zhang, G.S. Li, H.B. Wang, K.M. Chan, J.G. Yu, *Cryst. Growth Des.* 10 (2010) 1130–1137.
- [3] A. Feldhoff, C. Mendive, T. Bredow, D.W. Bahnemann, *Chem. Phys. Chem.* 8 (2007) 805–809.
- [4] X.N. Wang, B.B. Huang, Z.Y. Wang, X.Y. Qin, X.Y. Zhang, Y. Dai, M.H. Whangbo, *Chem. Eur. J.* 16 (2010) 7106–7109.
- [5] M. Apino, M. Takeuchi, *J. Catal.* 216 (2003) 505–516.
- [6] W. Choi, A. Termin, M.R. Hoffmann, *J. Phys. Chem.* 98 (1994) 13669–13679.
- [7] Y. Li, T. Wang, S. Peng, *Acta Phys.-Chim. Sin.* 20 (2004) 1434–1439.
- [8] J. Zhao, T. Wu, K. Wu, *Environ. Sci. Technol.* 32 (1998) 2394–2400.
- [9] V. Subramanian, E. Wolf, P.V. Kamat, *J. Phys. Chem. B* 105 (2001) 11439–11446.
- [10] V. Keller, P. Bernhardt, F. Garin, *J. Catal.* 215 (2003) 129–138.
- [11] Y.T. Kwon, K.Y. Song, W.L. Lee, G.J. Choi, Y.R. Do, *J. Catal.* 191 (2000) 192–199.
- [12] H. Tade, A. Kokubu, M. Iwasaki, S. Ito, *Langmuir* 20 (2004) 4665–4670.
- [13] S.S. Kim, S.C. Hong, *J. Air Waste Manag. Assoc.* 62 (2012) 362–369.
- [14] V.C. Papadimitriou, V.G. Stefanopoulos, M.N. Romanias, P. Papagianakopoulos, K. Sambani, V. Tudose, G. Kiriakidis, *Thin Solid Films* 520 (2011) 1195–1201.
- [15] A.L.J. Pereira, L. Gracia, A. Beltran, P.N. Lisboa-Filho, J.H.D. da Silva, J. Andres, *J. Phys. Chem. C* 116 (2012) 8753–8762.
- [16] G. Marci, L. Palmisano, A. Aclafani, A.M. Venezia, R. Campostrini, G. Carturan, C. Martin, V. Rives, G. Solana, *J. Chem. Soc. Faraday Trans.* 92 (1996) 819–821.
- [17] J.X. Li, J.H. Xu, W.L. Dai, H.X. Li, K.N. Fan, *Appl. Catal. B* 82 (2008) 233–243.
- [18] W.Q. Fang, X.Q. Gong, H.G. Yang, *J. Phys. Chem. Lett.* 2 (2011) 725–734.
- [19] T. Tachikawa, S. Yamashita, T. Majima, *J. Am. Chem. Soc.* 133 (2011) 7197–7204.
- [20] J. Rodriguez-Carvajal, *Physica B* 192, (1993) 55. FULLPROF: A program for Rietveld, Profile Matching and Integrated Intensities Refinement of X-ray and/or Neutron Data, Laboratoire Leon Brillouin, CEA-Saclay, France.
- [21] Y.F. Li, Z.P. Liu, L. Liu, W. Gao, *J. Am. Chem. Soc.* 132 (2010) 13008–13015.
- [22] P. Hohenberg, W. Kohn, *Phys. Rev.* 136 (1964) B864–B871.
- [23] W. Kohn, L.J. Sham, *Phys. Rev.* 140 (1965) A1133–A1138.
- [24] P. Giannozzi et al., <http://www.quantum-espresso.org>
- [25] K.A. Brueckner, J.L. Gammel, H. Weitzner, *Phys. Rev.* 110 (1958) 431–445.
- [26] ISO/DIS 22197-1 Fine ceramics (advanced ceramics, advanced technical ceramics). Test method for air-purification performance of semiconducting photocatalytic materials. Part 1. Removal of nitric oxide.
- [27] M.V. Sofianou, C. Trapalis, V. Psycharis, N. Boukos, T. Vaimakis, J.G. Yu, W.G. Wang, *Environ. Sci. Pollut. Res.* 19 (2012) 3719–3726.
- [28] C. Greaves, *J. Appl. Cryst.* 18 (1985) 48–50.
- [29] J.I. Langford, D. Louër, *J. Appl. Cryst.* 15 (1982) 20–26.
- [30] S. Paul, P. Cherti, A. Choudhury, *J. Alloy Compd.* 583 (2014) 578–586.
- [31] K.X. Hu, D. Zhang, B. Su, T.W. Button, J.P. Jones, *Microsci. Microanal.* 11 (2005) 1728–1729.
- [32] S.J. Dillon, M.P. Harmer, *J. Am. Ceram. Soc.* 89 (2006) 3885–3887.
- [33] J.K. Burdett, T. Hughbanks, G.J. Miller, J.W. Richardson, J.V. Smith, *J. Am. Chem. Soc.* 109 (1987) 3639.
- [34] Q.J. Xiang, K.L. Le, J.G. Yu, *Appl. Catal. B Environ.* 96 (2010) 557–564.
- [35] M. Naeem, S.K. Hasanain, M. Kobayashi, Y. Ishida, A. Fujimori, S. Buzby, S.I. Shah, *Nanotechnology* 17 (2006) 2675–2680.
- [36] T. Siva Rao, T. Abdo Segne, T. Susmitha, A. Balaram Kiran, C. Subrahmanyam, *Adv. Mater. Sci. Eng.* 2012 (2012) 1–9.
- [37] P. Peshev, M. Khrussanova, D. Chakarov, M. Terzieva, Ts. Marinova, *Mater. Res. Bull.* 24 (1989) 207–212.
- [38] P.R. Ettireddy, N. Ettireddy, S. Mamedov, P. Boolchand, P.G. Smirniotis, *Appl. Catal. B* 76 (2007) 123–134.
- [39] J.C. Carver, G.K. Schweitzer, T.A. Carlson, *J. Chem. Phys.* (1972) 973–982.
- [40] D.A. Pena, B.S. Uphade, P.G. Smirniotis, *J. Catal.* 221 (2004) 421–431.
- [41] E.L. Simmons, *J. Mod. Opt.* 19 (1972) 10 845–10 851.
- [42] H.Y. Li, D.J. Wang, H.M. Fan, T.F. Jiang, X.L. Li, T.F. Xie, *Nano Res.* 5 (2011) 460–469.
- [43] M.V. Sofianou, V. Psycharis, N. Boukos, T. Vaimakis, R. Dilert, D. Bahnemann, C. Trapalis, *Appl. Catal. B: Environ.* 142–143 (2013) 761–768.
- [44] M.V. Sofianou, T. Vaimakis, C. Trapalis, *Nanosci. Nanotech. Lett.* 5 (2013) 1–5.
- [45] R. Wanbayor, V. Ruangpornvisuti, *J. Mol. Struct.-Theochem.* 52 (2010) 103–108.
- [46] T. Sano, N. Negishi, K. Uchino, J. Tanaka, S. Matsuzawa, K. Takeuchi, *J. Photochem. Photobiol., A* 160 (2003) 93–98.
- [47] Z.Y. Liu, X.T. Zhang, S.S. Nishimoto, T. Murakami, A. Fujishima, *Environ. Sci. Technol.* 42 (2008) 8547–8551.
- [48] I. Sopyan, M. Watanabe, S. Murasawa, K. Hashimoto, A. Fujishima, *J. Photochem. Photobiol., A* 98 (1996) 79–86.
- [49] H.M. Hou, H. Miyafuji, S. Saka, *J. Mater. Sci.* 41 (2006) 8295–8300.
- [50] Z.Q. Yu, S.S.C. Chuang, *J. Catal.* 246 (2007) 118–126.
- [51] D. Meroni, S. Ardizzone, G. Capelletti, C. Oliva, M. Ceotto, D. Poelman, H. Poelman, *Catal. Today* 161 (2011) 169–174.